Chapter 7

Nonequilibrium Phase Transformations in Cuprates†

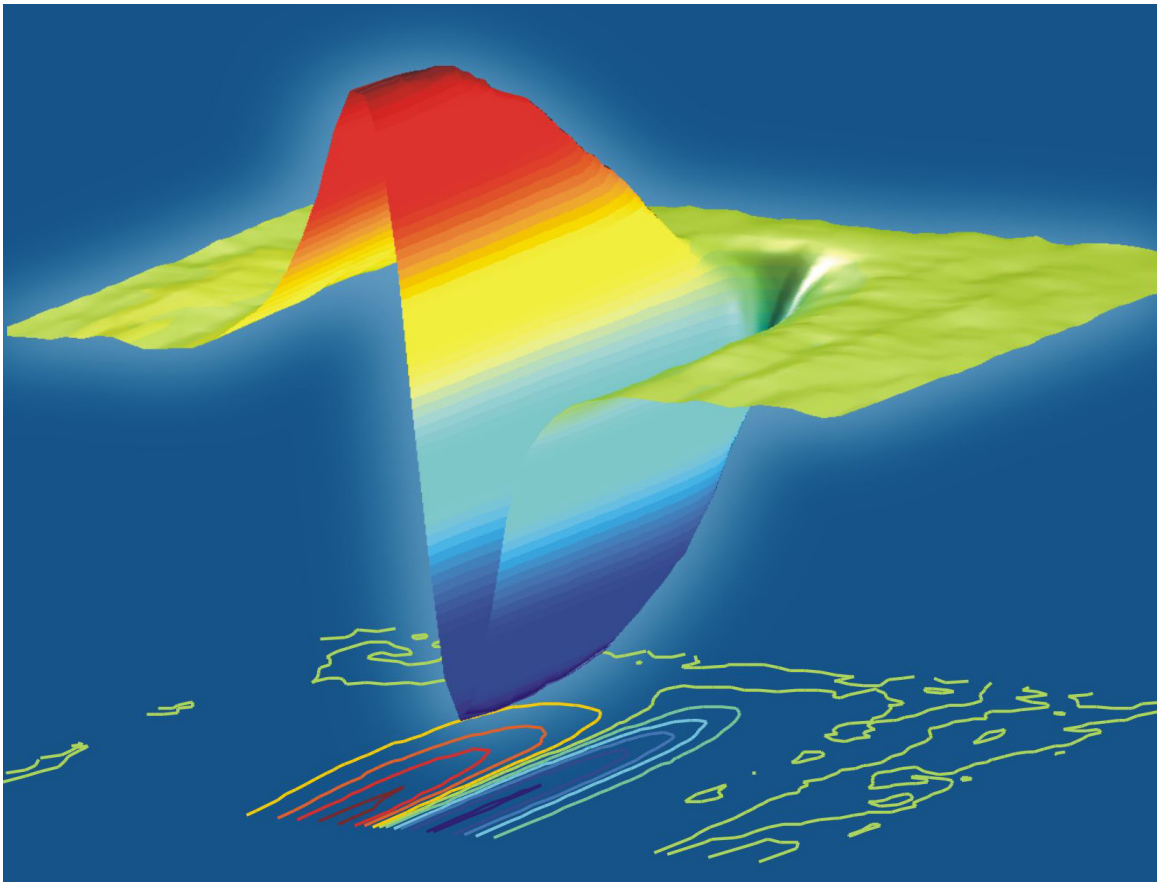

†adapted from N. Gedik, D.-S. Yang, G. Logvenov, I. Bozovic, A. H. Zewail, *Science* **316**, 425 (2007).

Introduction

The physical and chemical properties of materials can be altered as a result of the generation of metastable structures (*1*), electronic and/or structural modifications (*2, 3*), and phase transitions (*4*). For the latter, much of the work has been done on solids at equilibrium, namely when temperature or pressure becomes the variable of change. In contrast, transient structures of nonequilibrium phases, which are formed by collective interactions, are elusive and less studied because they are inaccessible to conventional studies of the equilibrium state. Initiated by photons, the structural changes underlying such transitions involve charge redistribution and lattice relaxation culminating in a process termed a photoinduced phase transition (*5-7*). In order to understand the nature of these optically dark phases, it is important to observe the structural changes with the use of time-resolved methods, especially ultrafast electron microscopy (*8-10*), electron diffraction (*10-12*), and x-ray absorption and diffraction (*13-17*). In this chapter, the direct observation of the nonequilibrium structural phase transition in superconducting cuprates is reported.

Materials and Experimental Section

The material that we chose to study is oxygen-doped $La_2CuO_{4+\delta}$ (LCO); although the undoped material is an antiferromagnetic Mott insulator, doping confers superconductivity below the critical temperature (T_c) and metallic properties at room temperature. Thin films were grown on a $LaSrAlO_4$ substrate by means of an atomic-layer molecular beam epitaxy (MBE) system (*18*). The films under study were characterized during growth by reflection high-energy electron diffraction and *ex situ* by atomic force microscopy (AFM), x-ray diffraction, and measurements of resistivity and

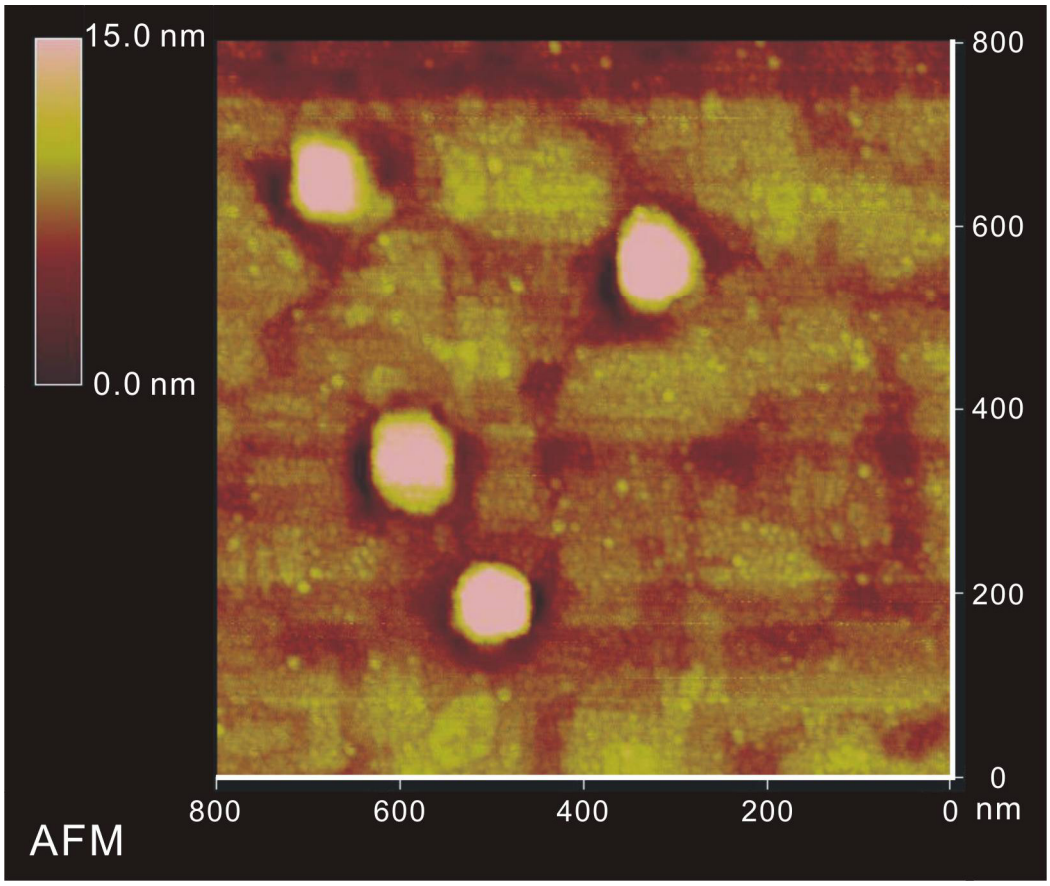

Fig. 1. AFM image of the topography of the LCO surface. The scan range is 800 nm by 800 nm. The surface of the film is atomically flat except for a few three-dimensional islands seen as circular white regions in the image. They are cylindrically shaped with a base diameter of ~50 nm and a typical height of ~20 nm. These structures are small LCO islands epitaxially aligned with the underlying cuprate film.

magnetic susceptibility as a function of temperature. The products are single-crystal films, and AFM shows atomically smooth surfaces (root-mean-square roughness in the 0.3- to 0.6-nm range). In few films, we observed some surface roughness, in the form of some islands with a typical width of 50 to 200 nm and a height of ~20 nm, small enough for transmission electron diffraction to be observed (Fig. 1). The islands were verified to have the same crystal structure and conductivity as those of the single crystal, as

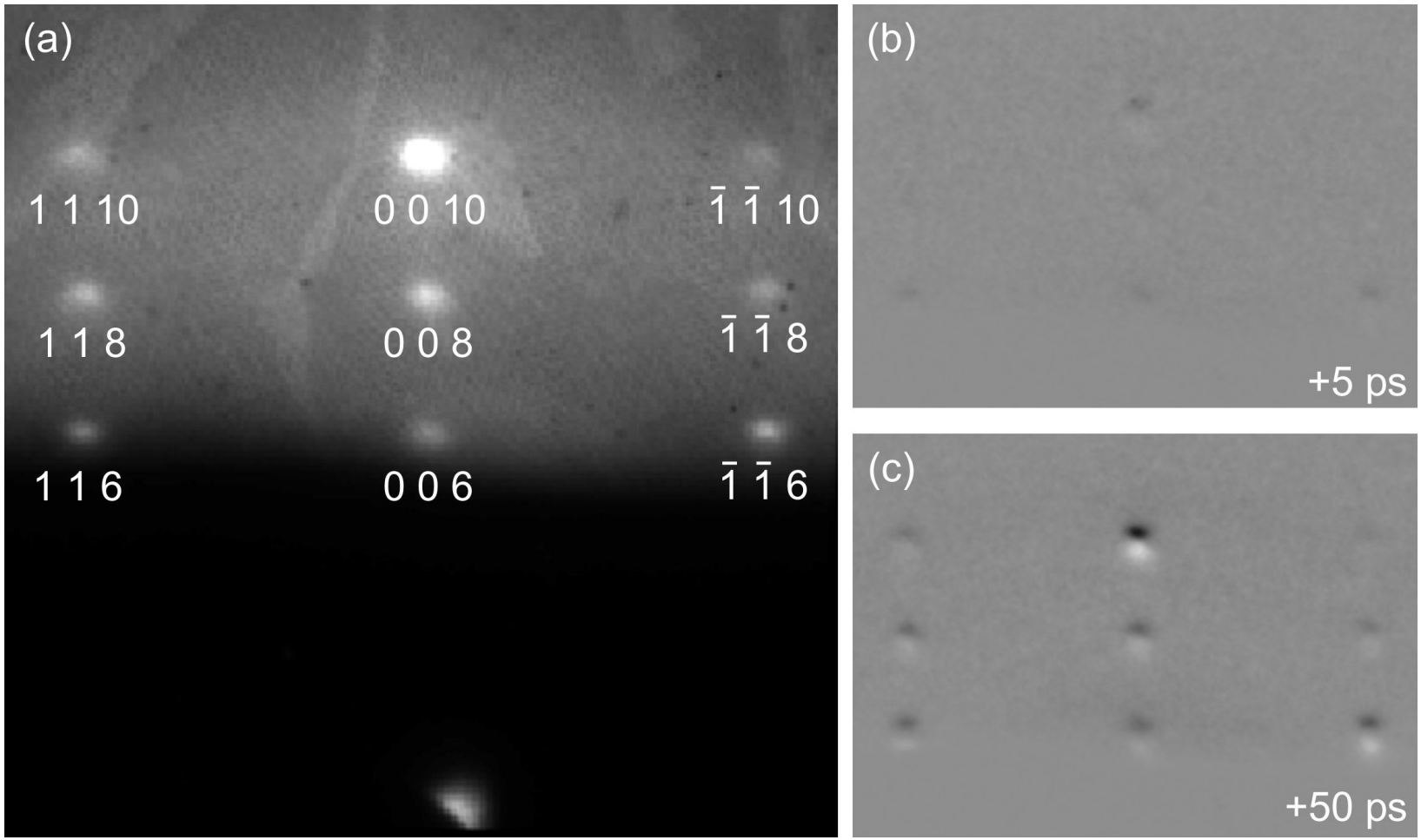

Fig. 2. (a) Diffraction pattern of $La_2CuO_{4+\delta}$ obtained at equilibrium. The pattern is transmission-like, and the spots are indexed with the use of the tetragonal unit cell. (b and c) Diffraction difference images (referenced to panel a) at +5 ps and +50 ps, respectively.

evidenced by measurements of the lattice constants and by electric force microscopy, respectively. One such film, with a thickness of 52 nm and a critical temperature $T_c \sim 32$ K, was chosen for the present study.

Ultrafast electron crystallography (UEC) has been established as a method for studying surfaces and nanometer-scale materials with atomic-scale resolutions. The sample was photoexcited by 800-nm light pulses (with a temporal width of 120 fs) and probed by electron packets generated via the photoelectric effect. In order to observe lower-order Bragg diffractions from the material, the incidence angle of electrons ($\theta/2$) is set typically between ~1º and 2º. The scheme of pulse front tilting (*19*) was used for all experiments reported here to achieve the necessary time resolution and sensitivity. To tune the temperature and incidence angle (for rocking curve measurements), we mounted the sample on a metallic holder coupled to a cryostat that was capable of reaching 10 K, which in turn was placed on a goniometer with an angular precision of 0.005°.

Results and Analysis

In Fig. 2a, the static diffraction pattern obtained at room temperature is shown with no excitation. From the observed Bragg spots in s space, where $s = (4\pi/\lambda)\sin(\theta/2)$, we indexed the pattern using the tetragonal unit cell of the cuprate $La_2CuO_{4+\delta}$. Analysis of the diffraction patterns for different zone axes gives lattice constants of $a = b = 3.76$ Å and $c = 13.1 \pm 0.1$ Å, which are in agreement with the x-ray diffraction measurements made on the same film ($a = b = 3.755$ Å and $c = 13.20$ Å). The error range in the determination of the absolute values of the lattice constants comes from the uncertainty in determining the sample-to-camera distance. However, relative changes can be measured with much better accuracy, reaching below 0.01 Å (or 0.001 Å through fitting).

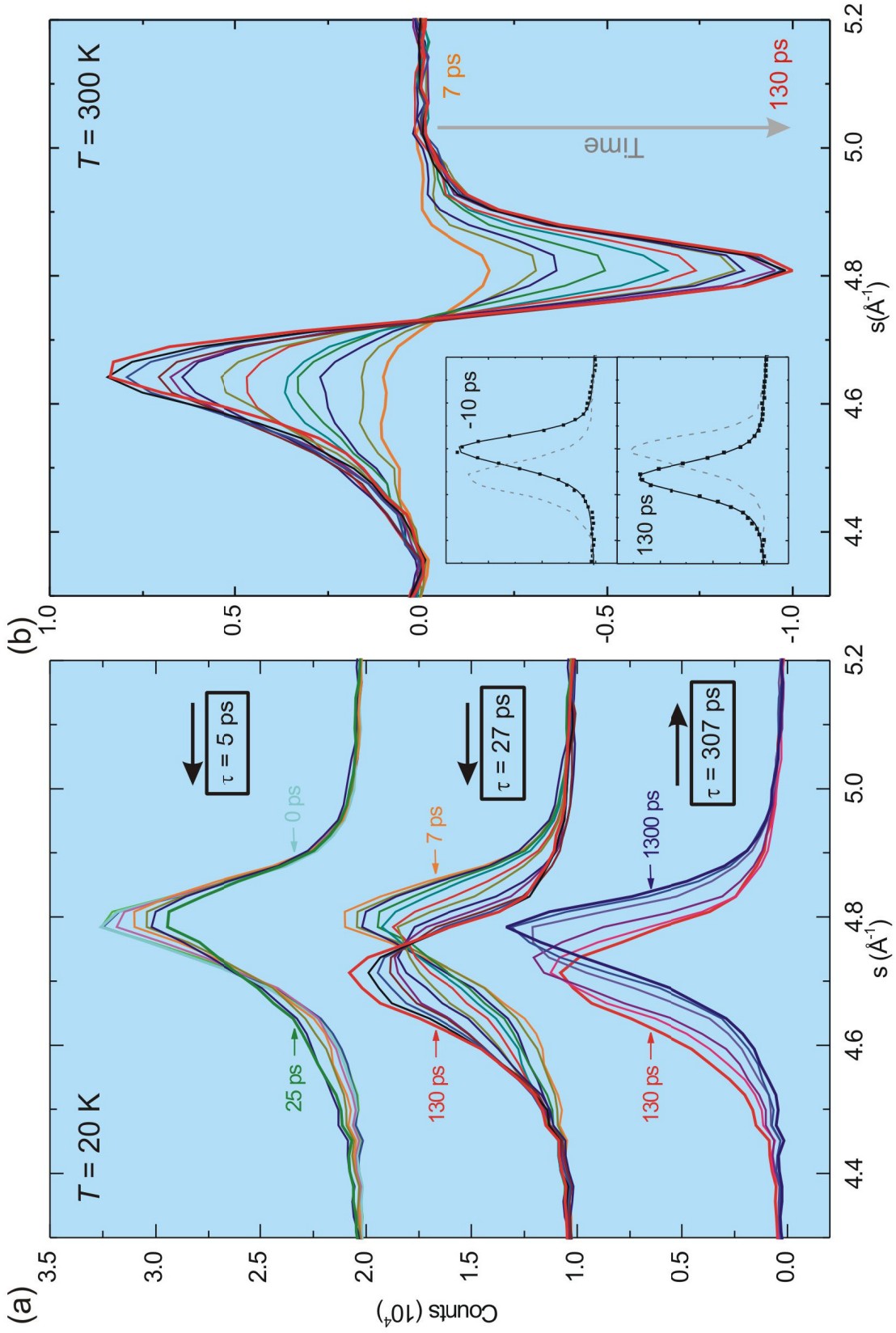

(See next page for the figure caption.)

Fig. 3. Diffraction evolution with time. (a) Profiles of the (0 0 10) Bragg spot along the *c*-axis direction at different times. The fluence is 20.6 mJ/cm^2 and temperature is 20 K. A small background (determined experimentally from a nearby diffuse region on the CCD) was subtracted. Similar diffraction results were obtained at room temperature and at $T = 100$ K. Three distinct behaviors are shown: between 0 and 25 ps [top; time (t) = –34, –11, 0, 1, 7, 13, 19 and 25 ps]; between 7 and 130 ps (middle; $t = 7$, 13, 19, 25, 34, 43, 52, 61, 70, 79, 88, 101, 130 ps), there is a prominent structural isosbestic point at $s = 4.76$ Å^{-1}; and on a much longer time scale (bottom; $t = 130$, 191, 266, 516, 816, 1300 ps), the restructuring back to the ground state is observed. For the recovery, the curves continuously shift to higher s values (shorter c) without crossing. The black arrows indicate the direction of temporal evolution for the formation and restructuring of the transient phase. (b) Difference profiles of the (0 0 10) Bragg spot along the *c*-axis direction at different times, referenced to the negative time frame. The fluence is 20.6 mJ/cm^2 and temperature is 300 K. The structural isosbestic point is clearly seen near zero intensity, and the depletion of the initial structure and the growth of the transient structure are apparent. The inset shows the Voigt-type function fit for the diffraction intensity profiles at two different times: –10 and +130 ps.

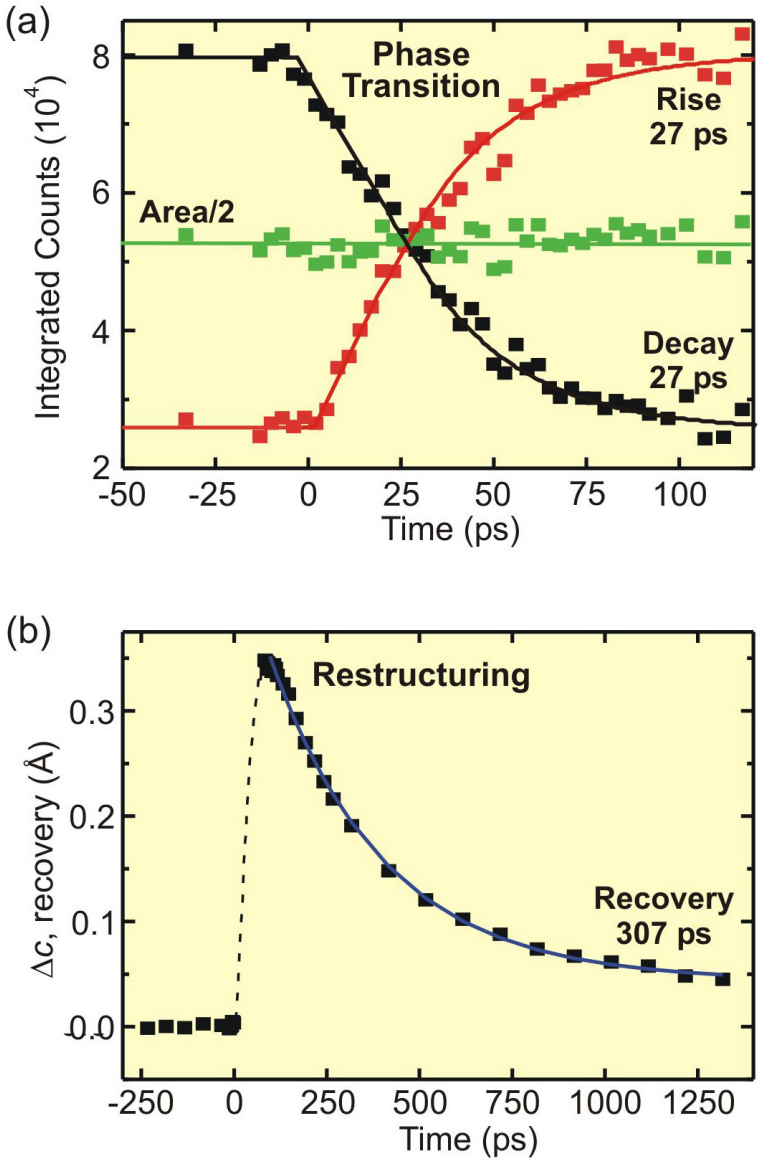

Fig. 4. Time scales of structural changes. (a) Integrated intensity decay (black squares) and rise (red squares) of the structural isosbestic behavior shown in Fig. 3b. The green squares show, at given times, the total integrated intensity divided by two. The average of the black and red squares yields the green squares. The lines are guide to the eye. The intensity decay and rise give a time constant of 27 ps; the initial 5-ps range is not included. (b) Recovery of the *c*-axis lattice constant change (black squares). Dashed line indicates an average *c*-axis lattice spacing in the phase-transition region where more than one state is involved. The blue curve is a fit to an exponential decay with a time constant of 307 ps and a constant offset of 0.04 Å.

Structural dynamics of the material were obtained by recording the diffraction frames at different times, before and after the arrival of the optical excitation pulse. In Fig. 2, panels b and c, two representative diffraction difference patterns are shown. These difference patterns display the changes induced by the initiation pulse; they are frames obtained at the specified times and referenced, by subtraction, to a frame at negative time (i.e., before optical excitation). At 1.55 eV, the femtosecond pulse only excites the material because the substrate is transparent to the 800-nm light; the penetration depth of the laser pulse in the material is 143 nm (*20*), which far exceeds that of the probing electron pulse (~10 nm). Therefore, the observed structural dynamics can only originate from the cuprate film.

After the femtosecond initial excitation, the observed Bragg spots shift downward (along the *c* direction), indicating an increase in the *c*-axis lattice constant. For other Bragg spots, the shift scales correctly with the order of diffraction. For example, the shift (Δs in s space) of the (008) spot is 80% of that of the (0 0 10) spot, in accord with the relationship $\Delta c/c = -\Delta s/s$. (We measured no change in the position of the direct electron beam on the CCD camera.) The observed changes are on three different time scales, characterized by time constants of 5 ps and 27 ps for the formation of the transient phase and 307 ps for structural recovery (see Figs. 3 and 4).

The change with time is striking. In Fig. 3a, we plot the vertical profiles of the (0 0 10) Bragg spot along the *c* direction at different times. At negative times, the Bragg peak is centered at an s value corresponding to the equilibrium c value of the lattice: $s = 10\,|\boldsymbol{c}^*| = 4.80$ Å^{-1}, where $|\boldsymbol{c}^*| = 2\pi/c = 0.480$ Å^{-1}. The structure at positive times evolves first in a few picoseconds and then changes drastically in tens of picoseconds; for example, at 120 ps after the excitation, the peak becomes centered at a lower value

($s = 4.70$ Å^{-1}) corresponding to a huge increase (~2.5%) in the *c*-axis lattice constant. We studied the material behavior at three different temperatures, 20, 100 and 300 K.

The unexpected feature of Fig. 3 is that, before restructuring, all of the curves obtained at different times cross at a single point, $s = 4.76$ Å^{-1}, at the fluence of 20.6 mJ/cm^2. What was expected, as observed in semiconducting materials (Chs. 4 and 5), was that the peak would shift continuously while the intensity decreased with time. Neither behavior is observed here at the high signal-to-noise level achieved (Figs. 3 and 4). Thus, this intensity sharing with a common crossing point, as shown below, indicates a structural transition from the initial phase to a new one. Such a crossing behavior in spectroscopy would be termed an isosbestic point, corresponding to the spectral position where two interconverting species have equal absorbance; regardless of the populations of the two states, the total absorption at the isosbestic point does not change.

For the structural dynamics studied, we observe the interconversion between two structures with different *c*-axis lattice constants and, for this reason, we term this point the structural isosbestic point. At this particular *s* value, the two structures involved are diffracting equally, and their coexistence is evidenced in the temporal changes. The influence of the time-independent instrumental response function (from the electron beam size) has been taken into consideration. For the case of two interconverting structures with Gaussian intensity profiles, it can be shown mathematically that instrumental broadening only modifies the widths, but structural isosbestic points remain robust. The behavior of interconversion is clearly illustrated in Fig. 3b, where we display, as a function of time, the depletion of the initial structure and the growth of the transient-phase structure. The data, which was acquired over the same time delays as those of Fig. 3a (middle), were obtained by referencing all frames to the diffraction

profile of the equilibrium structure at negative time. In the inset of Fig. 3b, the actual diffraction profile of the (0 0 10) Bragg spot is shown at two different times, –10 and +130 ps, with each profile fitted to a Voigt-type function.

The decay of the initial structure and the formation of the new structure are quantified by integrating the intensity underneath the (0 0 10) diffraction curves. For the diffraction data obtained in Fig. 3b, the green line in Fig. 4a is the total integrated intensity divided by two. The fact that it is not changing with time rules out the involvement of intensity-depletion processes, such as those described by the Debye–Waller mechanism (Eq. 16 of Ch. 2); in that case, the mean vibrational displacement of the atoms would have increased and caused a decrease in diffraction intensity, contrary to what is observed. Moreover, because the linear expansion coefficient is $\alpha_l \leq 1.0\times10^{-5}\ \mathrm{K}^{-1}$ (*21*), a 2.5% increase in the lattice constant would correspond to an unphysical rise of 2500 K in the lattice temperature. The black and red curves are the total integrated intensity to the right and left of the crossing point in Fig. 3b, respectively. They reflect the population change of the initial structure and that of the new one. The population of the initial structure (black curve in Fig. 4a) decays with a time constant of 27 ps, describing the growth of the transient phase.

The restructuring at longer times is depicted by Δc as a function of time in Fig. 4b. The dashed line near time zero represents an average value of c for the structures that are present. With no crossing, the value of Δc decreases and reaches an asymptote at ~1 ns. This restructuring after the phase transition can be described by an exponential decay with a time constant of 307 ps with an offset of about 0.04 Å. Accordingly, even after 1 ns, the restructuring is incomplete and, for complete equilibration, a much longer time scale is required. Some contribution from a temperature rise induced by the laser pulse

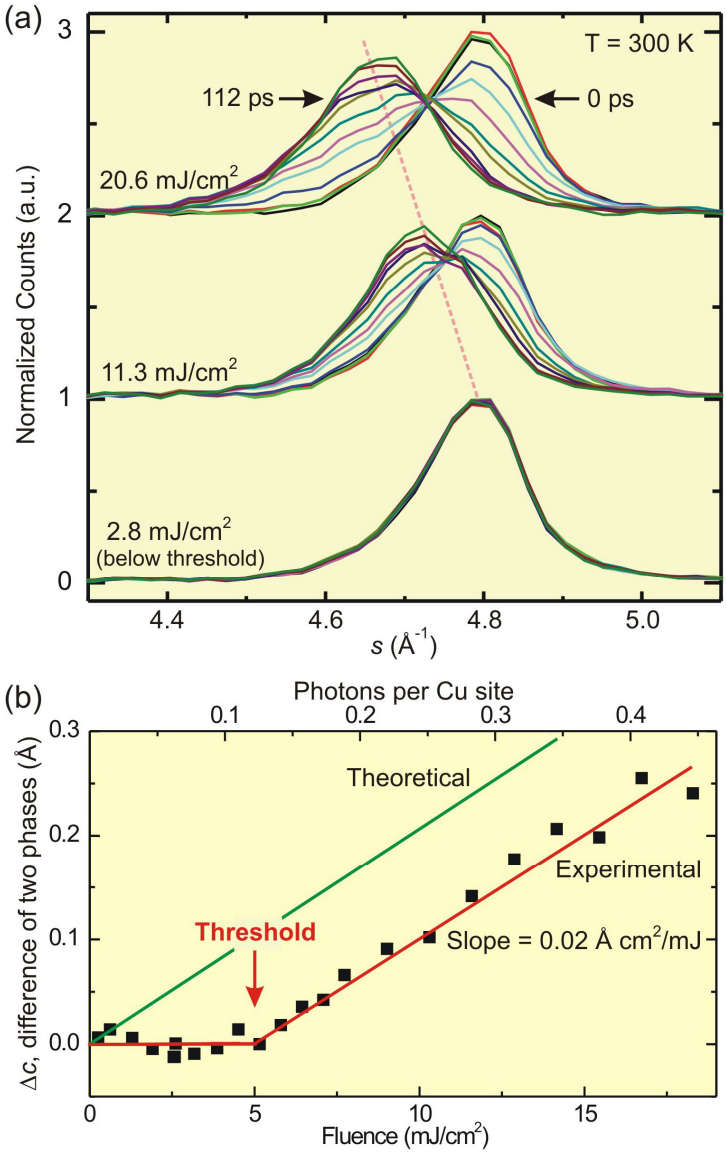

Fig. 5. Threshold behavior and fluence dependence. (a) Typical diffraction profiles at three fluences, 2.8 (below threshold), 11.3 and 20.6 mJ/cm^2 (above threshold). The profile for the equilibrium phase remains at the same s value, whereas that for the transient phase (indicated by the dashed line) shifts toward a lower s value as the fluence increases. The structural isosbestic point is robust. All peaks are normalized to the $t = 0$ peak maximum at each fluence; the displacement for different fluence is in arbitrary units (a.u.). (b) The difference of the c-axis lattice constant between the two phases, $\Delta c_{max} = c(130\ \text{ps}) - c(-85\ \text{ps})$, as a function of fluence. The horizontal axis on the top shows the number of photons absorbed per copper site as calculated with the use of the linear absorption coefficient. There is a clear threshold at 5 mJ/cm^2. Above the threshold, Δc increases linearly with fluence with a slope of 0.02 Å/(mJ/cm^2) (red line). The theoretical calculations (green line) yield a slope that is in good agreement with that obtained from the experimental data.

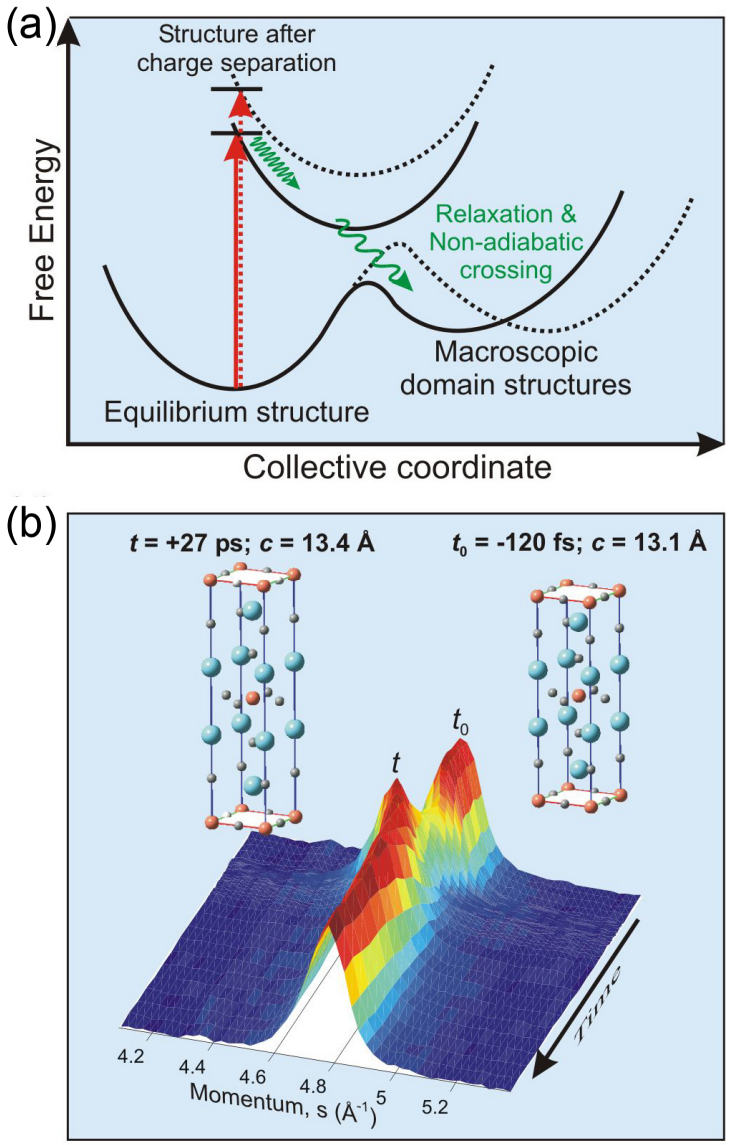

Fig. 6. Trajectories of structural changes. (a) Free-energy curves. The initial charge-transfer excitation leads, after lattice relaxation and nonadiabatic crossing (*5*-*7*), to the new structure, in this case with the charge being transferred from oxygen to copper. Further increase in the energy of the charge-transfer subsystem results in displacement of the curves (dotted curves) (*24*). Red arrows indicate excitation, and green arrows indicate the relaxation and nonadiabatic processes. (b) The temporal evolution of the (0 0 10) Bragg diffraction in the *s*–*t* space is shown as a three-dimensional plot (bottom). The initial structure of $La_2CuO_{4+\delta}$ before time zero (t_0) is shown on the upper right corner [copper (red spheres), oxygen (grey spheres) and lanthanum (blue spheres)]. After the phase transition, the new structure is indicated with a higher *c*-axis lattice constant (upper left corner). The change is exaggerated for illustration purposes. As restructuring takes place, the positions of the Bragg diffraction spots move continuously toward the equilibrium *s* values on a slower time scale.

may be present; the 1-ms delay between pulses is sufficient for the cooling of the sample.

Another notable feature of this structural phase transition is its dependence on the fluence of the initiating pulse. The maximum lattice constant change, $\Delta c_{max} = c(130\ \text{ps}) - c(-85\ \text{ps})$, is shown in Fig. 5, panels a (for the profiles at three typical fluences) and b (for all the fluences studied). A threshold at 5 mJ/cm^2 is observed, below which no structural change can be detected. Above this fluence value, the basic picture described above—a crossing point at initial times and continuous restructuring at long times—is robust (see Fig. 5a). The time scales do not change either. However, the lattice constant (c) of the transient-phase structure changes with the laser fluence (F) [i.e., $\Delta c_{max} = p\ (F - F_{th})$, where the slope $p = 0.02$ Å/(mJ/cm^2) and F_{th} is the threshold fluence].

Discussion: The Physical Picture

From the results of structures and dynamics observed in the cuprate superconductor, the following simple model is suggested. At 1.55 eV, the excitation pulse induces a charge transfer (Fig. 6a) from oxygen (O^{2-}) to copper (Cu^{2+}) in the *a*–*b* copper–oxygen planes (*22*). With the lattice relaxation being involved, the excitation is shared microscopically (exciton-type), and finally a transition to a transient phase is made (macroscopic domain). This transient phase requires a three-dimensional lattice ordering. The net charge distribution in the transient phase results in the weakening of interplanar Coulomb attractions, leading to expansion along the *c* axis. The behavior is nonlinear in that when the number of transformed sites is below a critical value, the macroscopic transition is not sustainable. The threshold, which has also been observed in organic crystals (*7*), reflects this need for cooperativity at the macroscopic scale. The crystal domain is at least 20 nm^2 (from the apparent peak width, Δs_w, which gives the minimum

coherence length); the maximum is determined by the 800-nm wavelength used. Symmetry breaking is not evident because charge transfer is in a plane perpendicular to the *c*-axis expansion, whereas, in Ref. 7, charge separation is along the axis of expansion.

At any fluence above the threshold, the interconversion is between two phases (isosbestic point). In order to account for the large magnitude of the expansion and its dependence on the fluence, a uniform charge distribution was considered, after the in-plane charge transfer from oxygen to copper. In the domains of the transient phase, the charges on copper and oxygen become $Q(\mathrm{Cu}) = 2 - \delta_p$ and $Q(\mathrm{O}) = -2 + \delta_p/2$, respectively, where δ_p is the transferred fractional charge determined by the number of photons absorbed per copper site; the changes refer to the copper–oxygen planes with the valence of all the other atoms remaining the same. The ionic cohesion energy $U(\boldsymbol{r}_1, ..., \boldsymbol{r}_N, \delta_p)$, where $\boldsymbol{r}_i$ ($i = 1, ..., N$) are the coordinates of the atoms in the unit cell, was then calculated as the sum of the Madelung energy and the core repulsion energy; the latter was modeled as the sum of binary repulsion terms in the standard Born–Meier form of $A_j \exp(-r_j/d_{\mathrm{BM}})$, where the index j enumerates the relevant nearest-neighbor pairs (O–O, Cu–O, and La–O), and A_j and d_{BM} are the pair-wise atomic constants (*23*). For the equilibrium structure ($\delta_p = 0$), the parameters were optimized to match the experimentally determined equilibrium distances and the known lattice elastic constants. For a given fluence (equivalent to δ_p), the cohesive energy $U(\boldsymbol{r}_1, ..., \boldsymbol{r}_N, \delta_p)$ was then calculated to determine the new crystal configuration by minimizing the potential energy. The calculations give the observed magnitude for the change along the *c* axis and the linear dependence on fluence, as shown by the green line in Fig. 5b. The agreement of the slope confirms the role of the charge distribution in the formation of the transient phase. A full dynamical theory must consider such a distribution as the system evolves in time. Electron transfer

theory predicts that an increase in free energy will lead to a shift of the potential (*24*) and to a further increase of the expansion (Fig. 6a).

The dynamical nature of the energy landscape is determined by these changes in the electronic distribution and by the nuclear motions. For other materials exhibiting neutral-to-charged domain transitions, Nasu (*5*) has elucidated the origin of local and global minima, which are reminiscent of macromolecular structures (*25*-*27*), on the ground-state potential surface. More than one local minimum state may exist as a result of nonadiabatic "covalent–ionic" interactions (*28*) between the two potentials involved (*5, 6*). The multidimensional nature of the landscape requires consideration of dynamical trajectories and the possible bifurcation (*29*), in this case with the *c*-axis changes defining a unique coordinate. In our results, the disparity in yield for the 5-ps and 27-ps time regimes may suggest that the dynamics involve bifurcation with two types of trajectories, those that are direct and lead to a large *c*-axis structural change (low yield), and those that concurrently involve expansion and lattice relaxation (high yield) (*29*).

Figure 6b depicts the observed trajectories in momentum–time space and the two structures, only with *c*-axis expansions. The anisotropy of expansion is due to the fact that the sample is free to expand along the surface normal direction, whereas in *a–b* planes, the laser-excited region is constrained by the surrounding unexcited region. Moreover, for in-plane charge transfer, the Coulomb repulsion is mainly interplanar, which results in a substantial expansion along the *c* axis with essentially no lattice change in the *a–b* planes.

Unlike the phase formation dynamics, the recovery is a continuous process of shrinking the *c*-axis value without crossing. In other words, after the femtosecond initial excitation and charge separation, the photoinduced phase transition can only recover

toward the equilibrium structure by charge recombination and lattice relaxation (Fig. 6a and Refs. 5–7). For electron transfer processes (*24*), the recombination occurs on a much longer time scale than that of the charge transfer. For the cuprate, the time scale is more than an order of magnitude longer than the formation time of the transient phase. Optical phonons may be involved, but when the temperature was lowered from $T = 300$ to 100 or 20 K, we observed essentially the same recovery time. These observations suggest the involvement of lattice (acoustic) phonons, because the Debye temperature for this material is 163 K (*30*). The observed decay time of 307 ps is very close to the lifetime (300 ps) of coherent acoustic waves observed in the same material (*31*).

Finally, the meaning of the threshold value for the cuprate is addressed. What was not expected was the absolute value of the threshold in relation to charge distribution. Knowing the value of the threshold (5 mJ/cm^2) and the absorption coefficient at 800 nm ($\alpha = 7\times10^4$ cm^{-1}) (*20*), we obtained a value close to 0.12 photon per copper site. For the doped material used, the fractional charge on a copper site is 0.16 at the optimal doping level for superconductivity. The implication of this similarity is that chemical and light-induced carrier doping may be related. If general, this implication is important for the prospect of light-mediated control. When cuprates are doped chemically, the optical conductivity shows that the spectral weight of the charge-transfer gap is transferred into the intragap region (Mott transition); the photoinduced optical reflectivity and absorption display a similar behavior (*22, 32*).

Conclusion

The combined atomic-scale spatial and ultrafast temporal resolutions of UEC enabled the direct observation of structural nonequilibrium phase transitions in

nanometer-scale materials. The macroscopic transient structures are undetectable by optical probes with wavelengths longer than lattice spacings; the time scales of optical response and structural changes are also very different. For the cuprate studied, the observed phase transition is the result of electronic charge redistribution and lattice collective interactions that form domains. The similarity of the apparent threshold for photon doping and the chemical doping required for superconductivity may have its origin in the nature of the photoinduced inverse Mott transition (*33*). With UEC, it is now possible to explore these phenomena for different chemical and photon dopings and in materials of varying structures (see Ch. 8).

References:

1. S. Ramdas *et al.*, *Nature* **284**, 153 (1980).
2. J. M. Thomas, *Phil. Trans. R. Soc. London Ser. A* **277**, 251 (1974).
3. N. Bloembergen, in *Laser ablation: Mechanisms and applications II,* J. C. Miller, D. B. Geohegan, Eds. (American Institute of Physics Conference Proceedings 288, Woodbury, New York, 1994), pp. 3-10.
4. R. W. Cahn, P. Haasen, E. J. Kramer, Eds., *Materials science and technology: A comprehensive treatment Vol. 5*, (VCH, New York, 1991).
5. K. Nasu, Ed., *Photoinduced phase transition* (World Scientific, Hackensack, NJ, 2004) and cited references therein.
6. M. Kuwata-Gonokami, S. Koshihara, Eds., *J. Phys. Soc. Jpn.* **75**, 011001~011008 (2006).
7. E. Collet *et al.*, *Science* **300**, 612 (2003).
8. M. S. Grinolds, V. A. Lobastov, J. Weissenrieder, A. H. Zewail, *Proc. Natl. Acad.*

Sci. USA **103**, 18427 (2006).

9. J. M. Thomas, *Angew. Chem. Int. Ed.* **44**, 5563 (2005).
10. A. H. Zewail, *Annu. Rev. Phys. Chem.* **57**, 65 (2006).
11. X. Zou, in *Electron crystallography: Novel approaches for structure determination of nanosized materials,* T. E. Weirich, J. L. Lábár, X. Zou, Eds. (Springer, Dordrecht, Netherlands, 2006).
12. B. J. Siwick, J. R. Dwyer, R. E. Jordan, R. J. D. Miller, *Science* **302**, 1382 (2003).
13. C. Bressler, M. Chergui, *Chem. Rev.* **104**, 1781 (2004).
14. A. Rousse, C. Rischel, J.-C. Gauthier, *Rev. Mod. Phys.* **73**, 17 (2001).
15. D. von der Linde, K. Sokolowski-Tinten, J. Bialkowski, *Appl. Surf. Sci.* **109-110**, 1 (1997).
16. M. Bargheer, N. Zhavoronkov, M. Woerner, T. Elsaesser, *Chemphyschem* **7**, 783 (2006).
17. A. Cavalleri, M. Rini, R. W. Schoenlein, *J. Phys. Soc. Jpn.* **75**, 011004 (2006).
18. I. Bozovic, *IEEE Trans. Appl. Supercond.* **11**, 2686 (2001).
19. P. Baum, A. H. Zewail, *Proc. Natl. Acad. Sci. USA* **103**, 16105 (2006).
20. M. Suzuki, *Phys. Rev. B* **39**, 2312 (1989).
21. J. D. Yu, Y. Inaguma, M. Itoh, M. Oguni, T. Kyômen, *Phys. Rev. B* **54**, 7455 (1996).
22. D. N. Basov, T. Timusk, *Rev. Mod. Phys.* **77**, 721 (2005).
23. B. Piveteau, C. Noguera, *Phys. Rev. B* **43**, 493 (1991).
24. R. A. Marcus, *Angew. Chem. Int. Ed.* **32**, 1111 (1993).
25. P. F. McMillan, D. C. Clary, *Phil. Trans. R. Soc. London Ser. A* **363**, 311 (2005).
26. P. G. Wolynes, J. N. Onuchic, D. Thirumalai, *Science* **267**, 1619 (1995).

27. C. M. Dobson, *Nature* **426**, 884 (2003).

28. A. Mokhtari, P. Cong, J. L. Herek, A. H. Zewail, *Nature* **348**, 225 (1990).

29. K. B. Møller, A. H. Zewail, *Chem. Phys. Lett.* **295**, 1 (1998).

30. K. Kumagai *et al.*, *Phys. Rev. Lett.* **60**, 724 (1988).

31. I. Bozovic *et al.*, *Phys. Rev. B* **69**, 132503 (2004).

32. J. D. Perkins, R. J. Birgeneau, J. M. Graybeal, M. A. Kastner, D. S. Kleinberg, *Phys. Rev. B* **58**, 9390 (1998).

33. A. Pergament, A. Morak, *J. Phys. A Math. Gen.* **39**, 4619 (2006).